Decadal Trends and Variability in Special Sensor Microwave / Imager (SSM/I)

Brightness Temperatures and Earth Incidence Angle

Hilburn, K. A. (*) and C.-L. Shie (+)

(*) Remote Sensing Systems

(+) UMBC/JCET, NASA/GSFC

Corresponding Author:

Kyle Hilburn

Remote Sensing Systems

444 10th Street, Suite 200

Santa Rosa, CA 95401

Tel.: (707) 545-2904 ext. 13

Fax: (707) 545-2906

Email: hilburn@remss.com

Abstract

This paper describes earth incidence angle (EIA) trends and variability in the Special Sensor Microwave / Imager (SSM/I) dataset and their effect on brightness temperature (T_B) . The entire Remote Sensing Systems (RSS) dataset is analyzed, including all six sensors operating from 1987-2009. The methodology used to calculate EIA is explained, and the variability of EIA is characterized. The main source of variability is the change in altitude over an orbit. However this is modulated by the precession of perigee that varies with a four month period. The physical relationship between EIA and T_B is explained with the RSS radiative transfer model. The relationship is not constant, but depends on the meteorological conditions in the satellite footprint. Since the satellites are gradually falling over time, EIA has a trend of -0.14°/decade. This produces a -0.3 K/decade trend in vertical polarization T_B. RSS has always handled EIA variations using its retrieval algorithms that are parameterized in terms of EIA. In order to use legacy algorithms that do not include EIA dependence, an algorithm to normalize T_B to a nominal EIA is derived, and its accuracy is characterized. The algorithm performs very well in all meteorological conditions, and provides highly accurate decadal trends. The algorithm's impact on 500-m bottom-layer water vapor W_B retrievals is assessed. These retrievals are used by the Goddard Satellite-based Surface Turbulent Fluxes (GSSTF) dataset in the calculation of latent heat flux. The normalization algorithm increases the W_B trend by 0.16 mm/decade or 3.1%/decade.

1. Introduction

Accurate air-sea surface turbulent flux measurements are crucial to understanding the global water and energy cycles. The fluxes of sensible and latent heat from the ocean to the atmosphere are crucial terms in the surface energy budget. Evaporation from the ocean supplies roughly 85% of the atmospheric water vapor to the global water cycle. The flux of momentum from the atmosphere to the ocean drives ocean currents. The vastness of the ocean makes satellite remote sensing a valuable tool for global monitoring of these flux measurements. The need for accurate flux datasets led to the development of the Goddard Satellite-based Surface Turbulent Fluxes (GSSTF) dataset [*Chou et al.*, 1995, 1997, 2003; *Shie et al.*, 2009; *Shie*, 2010a]. Recently GSSTF was revived, and the Version-2b (GSSTF2b) dataset was officially released via the Goddard Earth Sciences (GES) Data and Information Services Center (DISC) in October 2010 [*Shie et al.*, 2010]. GSSTF2b provides the sensible heat flux, latent heat flux, surface wind stress, and other relevant air-sea parameters at 1°x1° spatial resolution and daily time resolution for the period July 1987 through December 2008. GSSTF2b uses improved input data to derive the fluxes, including updating to Remote Sensing Systems' (RSS) Version-6 Special Sensor Microwave / Imager (SSM/I) brightness temperature (T_B) climate data record. Fluxes in GSSTF2b agree better with ship observations than the preceding Version-2 (GSSTF2) due to the improved input data [*Shie*, 2010a, 2010b].

The latent heat flux in GSSTF is calculated using a bulk aerodynamic formula [*Chou et al.*, 1995, 1997, 2003]. This requires knowledge of the specific humidity at a reference height in the atmosphere, which is calculated using a second-order Empirical Orthogonal Function expansion of the vertical specific humidity profile [*Chou et al.*, 1995, 1997]. This technique solves for the specific humidity as a function of two parameters: the total column-integrated water vapor W and

the lowest 500-m bottom-layer water vapor W_B. RSS T_B data are used to calculate the bottom-layer water vapor W_B using the *Schulz et al.* [1993] relationship:

$$W_B\left(\text{mm}\right) = -59.339 + 0.3697 \cdot T_{19V} - 0.2390 \cdot T_{19H} + 0.1559 \cdot T_{22V} - 0.0497 \cdot T_{37V} \tag{1}$$

where brightness temperature has units of K. As discussed by *Chou et al.* [1997], the calculated specific humidity depends strongly on W_B but weakly on W, which is why W_B is of fundamental importance to the GSSTF dataset. The dependence of GSSTF latent heat flux on W_B is the subject of a separate paper [*Shie et al.*, in preparation].

In a trend analysis study [*Chiu et al.*, 2008] of oceanic evaporation datasets that included: GSSTF2 (which covers the period July 1987 – December 2000), Japanese Ocean Flux data sets with Use of Remote sensing Observations (J-OFURO), Hamburg Ocean Atmosphere Parameters and fluxes from Satellite data Version-2 (HOAPS2), and National Center for Environmental Prediction (NCEP) reanalysis; an increase in global-average surface latent heat flux (LHF) was commonly found in all four datasets for the period 1988-2000. The first set (Set1) of GSSTF2b showed a significant improvement (reduction) in the associated trend compared to the preceding GSSTF2 over the period 1988-2000; however, the trend in GSSTF2b-Set1 seemed to increase after 2000. A second set (Set2) of GSSTF2b was then produced [*Shie et al.*, 2010] by manually removing certain data from individual satellites (i.e., F08-F15) that contained relatively larger LHF trends. *Shie* [2010a,b] pointed out that the trend in LHF was mainly caused by W_B through the retrieved specific humidity, which is based on W_B. *Shie* further suggested that the trend found in W_B must be related to a trend in T_B through Equation (1). A preliminary investigation of the T_B impact on W_B has recently been presented by *Shie and Hilburn* [2011].

In order to confidently use GSSTF for further climate trend studies, a fundamental assessment of trends in W_B was performed. This assessment found larger than expected trends in

W_B and large intersensor offsets. Trends and offsets in W_B are directly attributable to trends and offsets in T_B according to Equation (1). Through collaboration between our two groups, these trends and offsets were determined to be due to the effect of SSM/I earth incidence angle (EIA) on T_B, which Equation (1) does not account for. Most algorithm developers today are aware of the EIA effect, and as a result, may see little need for discussing it in the published literature. For this reason, unfortunately, there is very little published literature on the subject. This paper is mainly intended for scientists who are users of satellite data, but are not satellite "experts" or part of the select group of algorithm developers. The purpose of this paper is to characterize how T_B depends on EIA, to characterize EIA variability in the SSM/I data record, and to provide a simple and accurate method for removing the EIA dependence from T_B. By "simple" we mean a method that does not require a time consuming major re-coding or reorganization of existing algorithms. We require accuracy across a broad range of physical circumstances and at a level that provides accurate trends on climate time scales.

The earth incidence angle θ is the angle between the satellite look vector (i.e., boresight vector) and the local vertical on the earth where the satellite is viewing. Details for how EIA is calculated in the RSS SSM/I dataset are provided in Section 3. Each SSM/I satellite has a different mean EIA and a gradual decreasing trend over time due to decreasing altitude from orbital drag. A complete characterization of EIA variations in the SSM/I dataset is provided in Section 4. The effect that EIA trends can have on satellite climate data records has long been recognized. For example, *Wentz and Schabel* [1998] discussed the effect of EIA trends on a 17-year lower-tropospheric temperature record from the Microwave Sounding Unit sensor.

The dependence of T_B on θ under typical conditions is illustrated in Figure 1. The overall relationship between T_B and θ is a function of θ itself, but the range of EIAs experienced by

SSM/I is limited, so the dependence of $\partial T_B / \partial \theta$ on θ is extremely small for SSM/I. Figure 1

shows $\partial T_B / \partial \theta$ when the atmosphere makes a minimal contribution (0 mm of water vapor) and

for typical conditions in the deep tropics (60 mm of water vapor). When the atmosphere is

negligible, $\partial T_B / \partial \theta$ is about 2 K/deg for vertical polarization (v-pol) and -1 K/deg for horizontal

polarization (h-pol). In the absence of an atmosphere, $\partial T_B / \partial \theta$ is given by just the change in

surface emissivity with θ. Since the specular Fresnel emissivity is the largest component of the

surface emissivity, the slopes of T_B versus θ for 0 mm of water vapor closely match the Fresnel

values. The differences between these curves are due to the non-specular wind-induced

emissivity component and oxygen absorption. For large amounts of water vapor, $\partial T_B / \partial \theta$

changes little for v-pol while it increases to 0.6 K/deg for h-pol. This is because the changes in

surface emission and atmospheric transmission with θ tend to cancel for v-pol, but add for h-pol.

The global mean value of h-pol $\partial T_B / \partial \theta$ is roughly 0 K/deg, which is why EIA has little effect

on h-pol T_B trends. A more detailed description of how $\partial T_B / \partial \theta$ depends on wind speed and

water vapor is given in Section 5. The calculations for Figure 1 assume no cloud liquid water, a

wind speed of 7 ms^{-1}, and sea surface temperatures of 0°C for the 0 mm vapor case and 28°C for

the 60 mm vapor case.

While it may be tempting to think of the T_B trends caused by EIA trends as "artifacts", they

are a real physical phenomenon that cannot accurately be removed by an intercalibration

procedure. There are two methods for handling the effects of EIA variations on geophysical

retrievals. The first way, which is the method used by RSS, is to parameterize the retrieval

algorithm in terms of EIA. The second way, which is developed in this paper, is to normalize the

T_B to a constant nominal value of EIA. The main difficulty in removing EIA effects outside of

the retrieval context is the dependence of $\partial T_B/\partial\theta$ on the scene. The scope of this paper is limited to where W_B retrievals are made: over the rain-free ocean where $\partial T_B/\partial\theta$ depends on sea surface temperature, surface wind speed and direction, columnar water vapor, and columnar cloud liquid water. Removing EIA effects over land or ice would require accurate EIA-dependent emissivity models for these surfaces. In addition to the emissivity models, it would also require information specifying environmental parameters such as: surface temperature; vegetation temperature, cover, type, and water content; soil type and moisture; the presence of snow cover or liquid water on the surface; and ice age.

EIA dependence in RSS retrieval algorithms is handled in the manner described by *Wentz* [1997] and *Wentz and Meissner* [2000], which follows the basic approach suggested by *Wilheit and Chang* [1980]. A large ensemble of ocean-atmosphere scenes is first assembled. Radiosonde data are used to specify vertical profiles of temperature and humidity in the atmosphere. Columnar cloud water ranging from 0 to 0.3 mm and distributed over various heights above the surface, ranging from 500 m to 2500 m, are superimposed on the radiosonde profiles. Values of surface wind speed ranging from 0 to 40 ms^{-1} are assigned to the ocean surface underneath the simulated atmospheres. Wind direction ranging from 0 to 360°, and sea surface temperature (SST) ranging in a ±5.5 K interval about the actual SST are also assigned. EIA is specified in 0.5° increments over a ±2.5° range about the nominal EIA of the sensor. The RSS radiative transfer model (Section 5) is then used to calculate T_B, and random noise is added to the simulated T_B. The brightness temperatures become the independent variable; and the SST, wind, vapor, and cloud become the dependent variables in a multiple linear regression. Linear, quadratic, and logarithmic functions of brightness temperature are included in the regression. The different EIA cases are treated separately; resulting in a table of retrieval coefficients that

depend on EIA. Finally, the retrieval algorithm takes the measured EIA and interpolates retrievals between the two closest EIA bins. A set of coefficients trained globally over all observations is used to obtain a first-guess SST, wind speed, water vapor, and cloud water. To account for nonlinearities between brightness temperature and the retrieved parameters, these first-guess values are used in a second-stage retrieval where the coefficients have been trained over regime specific conditions [*Chelton and Wentz*, 2005].

For the normalization approach, we are given the brightness temperature at a known earth incidence angle $T_B(\theta)$ and we want to calculate the brightness temperature at a nominal earth incidence angle $T_B(\theta_0)$. A Taylor series for $T_B(\theta)$ about θ_0 gives

$$T_B(\theta_0) = T_B(\theta) - \frac{\partial T_B}{\partial \theta}(\theta - \theta_0) \tag{2}$$

where the derivative $\partial T_B/\partial \theta$ is evaluated at θ_0. The higher order terms are very small because $\partial T_B/\partial \theta$ is almost constant in θ for the range of earth incidence angles encountered by SSM/I. The challenge then is how to specify the correct value of $\partial T_B/\partial \theta$ for each scene in the absence of information about the wind speed, columnar water vapor, and other environmental parameters. We have taken a similar approach as the only other published study dedicated to this subject [*Fuhrhop and Simmer*, 1996] by specifying $\partial T_B/\partial \theta$ based on the T_B itself. The idea is that since the measured T_B contain information about needed environmental parameters, $\partial T_B/\partial \theta$ can be specified using a multiple regression in the measured T_B. Our approach differs from *Fuhrhop and Simmer* [1996] in four ways. First, we regressed $\partial T_B/\partial \theta$ against the measured SSM/I T_B, and not simulated T_B. Doing so eliminated the need for an iterative approach. Second, *Fuhrhop and Simmer* [1996] constructed a simple radiative transfer model to predict

$\partial T_B / \partial \theta$. However we are using the RSS radiative transfer model (RTM), which has had the benefit of 35 years of development. This has the additional benefit of consistency, since it is the same RTM that was used to calibrate SSM/I. Third, while *Fuhrhop and Simmer* [1996] found no benefit from nonlinear terms in the multiple regression, we found that they did in fact improve the adjustment by removing small biases at high water vapor values. Finally, this paper considers the entire SSM/I data record and trends over time, while *Fuhrhop and Simmer* [1996] examined only one month of SSM/I data (June 1992) from F10 and F11. Our adjustment, the results of its application to SSM/I data, and an error budget are provided in Section 6. The implementation of this adjustment in a future version of GSSTF and its impact on GSSTF latent heat flux trends will be the subject of a separate paper by *Shie et al*.

2. Data

SSM/I was an extremely successful series of weather and climate monitoring sensors provided by the U.S. Defense Meteorology Satellite Program (DMSP). This series included the six satellites listed in Table 1 operating for the time periods specified. For F15, the end date is when the RADCAL beacon was turned-on, thus degrading the quality of the data and precluding its usage for climate studies [*Hilburn and Wentz*, 2008b]. The SSM/I sensor itself consists of 7 separate total-power radiometers, each simultaneously measuring the microwave emission from the Earth and atmosphere. The SSM/I measures vertical and horizontal polarization at 19.35, 37.0, and 85.5 GHz; and vertical polarization at 22.235 GHz. SSM/I has a 0.6 m offset parabolic reflector that focuses incoming radiation into a corrugated, broad-band, 7-port feedhorn. The reflector and feedhorn spin together about an axis parallel to nadir, with a rotation period of 1.9 s. Observations of the earth are taken during a 102.4º segment of the rotation, which gives a 1400 km wide swath on Earth's surface. The feedhorn also observes a hot reference load and a cold-space reflector during each rotation.

This study uses the Version-6 SSM/I brightness temperature dataset produced by RSS [*Wentz et al.*, 2007]. The Version-6 SSM/I climate data record is built on nearly 20 years of satellite intercalibration research at RSS. Version-1 was released in 1988 with the primary emphasis on data compression. Version-2 implemented more accurate geolocation and an antenna temperature along-scan correction [*Wentz*, 1991]. Version-3 was the first version to include more than one satellite, and it was the first version to include intersatellite calibration coefficients [*Wentz*, 1993]. With more satellites becoming part of the data record, Version-4 had a more careful intersatellite calibration that included diurnal variability and intra-orbit calibration variability. Version-4 also had refinements to the SSM/I pointing geometry to achieve better

geolocation. Version-5 introduced target factors in the calibration to remove errors correlated with the hot load temperature [*Mears et al.*, 2003]. Version-6 was released in 2006 after making improvements to the previous version's target factor approach, to account for F14 thermal variability and F10 attitude anomalies [see supporting online material with *Wentz et al.*, 2007].

In addition to T_B, this study uses RSS Version-6 geophysical retrievals of surface wind speed, columnar water vapor, and columnar liquid water from SSM/I. This study also requires knowledge of sea surface temperature (SST), and since SSM/I does not have a 6.9 GHz channel to retrieve global SST [*Gentemann et al.*, 2010], we made use of the NOAA/NCEP Reynolds optimal interpolation (OI) SST Version 2 product [*Reynolds et al.*, 2002]. Finally, we specify wind direction using the NCEP Global Data Assimilation System (GDAS) surface wind direction.

3. Geolocation Algorithm

Understanding how EIA is calculated is not just engineering details, but provides insight as to how and why EIA changes over time. This section shows that for a satellite flying a geodetic mission, as the DMSP satellites purportedly were, EIA depends primarily on two parameters: altitude, which changes over time; and the boresight nadir angle, which is fixed for each sensor. The RSS geolocation algorithm has been documented in *Wentz* [1991]. Geolocation was also discussed in *Meissner and Wentz* [2006] with the focus of calculating polarization rotation angle. This paper focuses on how the RSS geolocation algorithm calculates EIA.

Figure 2 shows the points (*E*, *S*, *G*), vectors ($\mathbf{R}, \mathbf{B}, \mathbf{C}$), angles ($\theta_n, \omega_n, \theta, \omega$), and three coordinate systems ($\mathbf{e}_1, \mathbf{e}_2, \mathbf{e}_3$; $\mathbf{s}_1, \mathbf{s}_2, \mathbf{s}_3$; $\mathbf{g}_1, \mathbf{g}_2, \mathbf{g}_3$) involved in geolocation. Point *E* is the center of the earth, *S* is the location of the satellite, and *G* is the location where the boresight vector $\mathbf{B}$ intersects Earth's surface. $\mathbf{R}$ is the satellite position vector, and $\mathbf{C}$ is the earth-boresight intersection position vector. The geocentric coordinate system (Fig. 2A) has its origin at the center of the Earth *E*, with unit vector $\mathbf{e}_1$ lying in the equatorial plane pointing towards the Greenwich meridian; $\mathbf{e}_2$ also lying in the equatorial plane and perpendicular to $\mathbf{e}_1$; and $\mathbf{e}_3$ pointing northward along Earth's axis of rotation. The satellite coordinate system (Fig. 2B) has its origin at the location of the moving satellite, with unit vector $\mathbf{s}_3$ pointing downward towards the satellite nadir point normal to the surface; $\mathbf{s}_1$ is perpendicular to $\mathbf{s}_3$ and lies in the orbital plane pointing in the direction of the spacecraft velocity; and $\mathbf{s}_2 = \mathbf{s}_3 \times \mathbf{s}_1$ completes the right-handed system. The local coordinate system (Fig. 2C) has its origin at the moving location of *G*, with unit vectors $\mathbf{g}_1$ pointing to local east; $\mathbf{g}_2$ pointing to local north; and $\mathbf{g}_3$ pointing upward normal to Earth's surface. Note that the orbit is plotted relative to the rotating earth, so the orbit

does not appear to make a closed ellipse; while in an inertial (non-rotating) reference frame, the orbit is a closed ellipse.

The boresight nadir angle θ_n (Fig. 2B) is the angle between the boresight vector $\mathbf{B}$ and satellite nadir vector $\mathbf{s_3}$, counterclockwise from the $\mathbf{s_3}$ axis. θ_n has a fixed value for each satellite around 45° (Table 1). The EIA θ (Fig. 2C) is the angle between the boresight vector $\mathbf{B}$ and the local normal $\mathbf{g_3}$ at the location where $\mathbf{B}$ intersects Earth's surface. The angle θ is taken counterclockwise from $\mathbf{g}_3$. Since Earth is an oblate spheroid, the vectors $\mathbf{s_3}$ and $\mathbf{g_3}$ which are normal to Earth's surface, do not point along $\mathbf{R}$ and $\mathbf{C}$ towards E, except at the equator. The boresight azimuth angle ω_n (Fig. 2B) is the angle in the $\mathbf{s_1}$-$\mathbf{s_2}$ plane between the boresight vector and $\mathbf{s_1}$ counterclockwise from $\mathbf{s_1}$. All SSM/I rotate clockwise looking down on the satellite from above. The value of ω_n at the first cell in each scan is fixed for each satellite, and ω_n decreases 1.6° for each of the 64 cells in a scan. Thus, as the reflector rotates a full 360°, it takes earth observations for a 102.4° segment, and uses parts of the remaining segment for cold and hot reference measurements. For F10 through F15 ω_n starts around 51°, and for F08 ω_n starts around -129° (Table 1). This is worth noting because the usual depiction of SSM/I geometry [*Hollinger*, 1990] is for F08, which was a backward looking instrument. All other SSM/I F10-F15 are forward looking instruments. Figure 2 is based on F13 data. The earth azimuth angle ω is the angle in the $\mathbf{g_1}$-$\mathbf{g_2}$ plane between the boresight vector and $\mathbf{g}_2$, defined clockwise from $\mathbf{g}_2$ (Fig. 2C). This is the same as the oceanographic convention for wind direction.

The EIA is calculated by the dot product of the boresight vector and the local surface normal vector

$$\cos(\theta) = -\hat{\mathbf{B}}_{(e)} \cdot \hat{\mathbf{g}}_{3(e)} \tag{3}$$

where $\hat{\mathbf{B}}$ is the boresight unit vector, $\hat{\mathbf{g}}_3$ is the local surface normal unit vector at location G, and

the subscripts (e) indicate that both vectors are given in the geocentric coordinate system

$(\mathbf{e}_1, \mathbf{e}_2, \mathbf{e}_3)$. Figure 2B shows that the boresight unit vector in the satellite coordinate system is

given by

$$\hat{\mathbf{B}}_{(s)} = \sin(\theta_n)\cos(\omega_n)\mathbf{s}_1 - \sin(\theta_n)\sin(\omega_n)\mathbf{s}_2 + \cos(\theta_n)\mathbf{s}_3 \tag{4}$$

This is transformed into geocentric coordinates using

$$\hat{\mathbf{B}}_{(e)} = \begin{bmatrix} B_1 \\ B_2 \\ B_3 \end{bmatrix} = \begin{bmatrix} X_1 & Y_1 & Z_1 \\ X_2 & Y_2 & Z_2 \\ X_3 & Y_3 & Z_3 \end{bmatrix} \hat{\mathbf{B}}_{(s)} \tag{5}$$

where the elements of the transformation matrix are given by (A1) in the Appendix. Next, the

location G where the boresight vector intersects the earth (Fig. 2A) has position vector $\mathbf{C}_{(e)}$,

which is calculated by

$$\mathbf{C}_{(e)} = \mathbf{R}_{(e)} + r\hat{\mathbf{B}}_{(e)} \tag{6}$$

where $\mathbf{R}_{(e)}$ is the position vector of the satellite in geocentric coordinates and r is the range

distance from the satellite to the earth. The satellite position vector is specified using the

procedure described by *Wentz* [1991], and the range distance is calculated using (A2) in the

Appendix. The elements of $\mathbf{C}_{(e)} = C_1\mathbf{e}_1 + C_2\mathbf{e}_2 + C_3\mathbf{e}_3$ are used to calculate the geodetic east

longitude λ_G and latitude Θ_G of location G

$$[\lambda_G, \Theta_G] = \left[\arctan\left(\frac{C_1}{C_2}\right), \arctan\left(\frac{\rho_e^2 C_3}{\rho_p^2 \sqrt{C_1^2 + C_2^2}}\right) \right] \tag{7}$$

14

where ρ_e and ρ_p are the equatorial (6378.137 km) and polar (6356.752 km) radii of the earth.

The geodetic latitude Θ_G is the angle between the equatorial plane and $\hat{\mathbf{g}}_{3(e)}$, which is normal to

earth's surface at G. Figure 2A shows that the local surface normal in geocentric coordinates is

$$\hat{\mathbf{g}}_{3(e)} = \cos(\Theta_G)\cos(\lambda_G)\mathbf{e}_1 + \cos(\Theta_G)\sin(\lambda_G)\mathbf{e}_2 + \sin(\Theta_G)\mathbf{e}_3 \tag{8}$$

Finally, EIA is calculated according to Equation (3) by taking the dot product of Equation (5) with Equation (8).

To get a more intuitive understanding of these complicated equations, consider the highly simplified example of a spherical earth with the boresight vector in the orbital plane. If θ_n is the boresight nadir angle, ρ is the radius of the earth, and h is the altitude of the satellite so that the distance from E to S is $R = \rho + h$, then the EIA is given by

$$\sin(\theta) = \left(1 + \frac{h}{\rho}\right)\sin(\theta_n) \tag{9}$$

(9) makes it clear that $\theta > \theta_n$ and that EIA will decrease if the satellite altitude decreases. Using the values of h and θ_n for each satellite in Table 1, (9) predicts θ with a mean absolute deviation from the actual mean θ of 0.004° for the six satellites. The SSM/I satellites lose roughly 10 km of altitude every decade. Assuming a typical altitude of 850 km and a typical boresight nadir angle of 45°, (9) predicts that a 10 km decrease in satellite altitude will produce a 0.1° decrease in EIA. The actual mean EIA trend in Table 1 is larger than this, with a value of -0.14°/decade, because the EIA offsets among the satellites add to the overall trend.

4. Characterization of Earth Incidence Angle Variations

In order to understand how EIA variations affect SSM/I T_B, it is important to first understand how EIA varies in the SSM/I data record. EIA variability is characterized by three main periodic modes as well as long-term trends. The most quickly varying mode, which we call the scanning mode, is due to the scanning sampling of the sensor. It has a very small amplitude of about 0.01° and a period of 1.9 seconds – the rotation rate of the reflector and feedhorn. The next most rapidly varying mode, which we call the orbital mode, is due to the oblateness of the earth and eccentricity of the orbit. This mode has an amplitude of about 0.1° and a period of about 101 minutes – the rotation rate of the satellite around the earth. The slowest mode of variability, which we call the perigee mode, is due to the precession of the orbital perigee through its position in the orbit. This mode also has an amplitude of about 0.1° and has a period of about 125 days. The perigee mode acts to modulate the orbital mode depending on the perigee phase. Finally, each satellite experiences long-term EIA trends on the order of -0.1°/decade due to their slowly changing orbits. In this section we first characterize the magnitude of EIA variability, and then we attribute that variability to each of the modes listed above. A simple mathematical model is provided to clarify the interaction of these modes.

Figure 3A shows histograms of EIA for each SSM/I sensor for the 1987-2009 time period. The total variability for all SSM/I over the entire data record is 1.6º with a mean of 53.2º. Excluding F10, the remaining five instruments vary over a range of 1.0º, but the variability for each individual satellite is roughly half of that: 0.54º. F10 has much larger variability than the other SSM/I due to its highly eccentric orbit, the result of a malfunction during launch. Each satellite has a different mean EIA, and these different means contribute to the overall decreasing trend in EIA in the SSM/I data record. Figure 3B shows global mean time series of EIA for each

SSM/I instrument. All of the satellites have decreasing trends in EIA ranging from -0.04°/decade for F11, to -0.19°/decade for F08 (Table 1). The mean of the trends weighted by satellite lifespan is -0.085°/decade. However, the trend for all satellites combined is -0.1415°/decade, showing how the different mean values for each sensor contribute to the overall data record trend. Global monthly mean EIA for F10 exhibits an oscillation with a four month period due to the perigee effect. Monthly global time series of EIA standard deviation (not shown) also exhibit a clear four month oscillation due to the perigee effect. When the orbit perigee is in phase with earth's oblateness, variability is enhanced; and when they are out of phase, variability is reduced.

Figure 4A-C provides an attribution of EIA variability into the scanning, orbital, and perigee modes. Figure 4D shows how combining these modes with the long-term trends in Figure 3B provides an accurate representation of EIA variability in the SSM/I dataset. Figure 4A shows the scanning mode by plotting the mean EIA versus along-scan cell number (1-64) with the scan average EIA removed for each scan. The curve in Figure 4A shows the mean for ascending orbital segments, and the cell numbers are reversed for descending passes. The EIA variability due to scanning is very small and nearly identical for all SSM/I instruments including F10. Since this variability source is so small, we will neglect it by using the scan-average EIA for the rest of the discussion in this section.

Figure 4B shows how EIA varies within the orbit. The orbit-averaged EIA is removed for each orbit, and the mean is plotted as a function of orbit position. Orbit position is defined as a fraction between 0 and 1, where 0 is at the beginning of the orbit and 1 is the end of the orbit. Orbit position is nearly equivalent to latitude, where 0 is near the equator, 0.25 is near the north pole, 0.5 is near the descending crossing of the equator, 0.75 is near the south pole, and 1 is at

17

the end of the orbit near the equator. Every latitude is associated with two orbit positions, one for the ascending pass and one for the descending pass. Figure 4B is the average over all perigee phases, and all SSM/I have similar mean behavior. EIA reaches a maximum over the southernmost portion of the orbit where the satellite is at its farthest position from the earth.

The precession of the perigee modifies the mean relationship shown in Figure 4B. If the earth were a perfect sphere, and in the absence of other perturbing forces, the orbit of a satellite would follow a fixed ellipse in the familiar way elucidated by Kepler. However, the earth bulges at the equator and is flatter at the poles, and this latitude dependence of geopotential causes the orbit to precess in two different ways. *Capderou* [2005] shows that if the geopotential is represented by a second degree expansion in spherical harmonics, then Lagrange's equations can be solved using a perturbation method to derive closed-form expressions for the rate of these two precessions. The second degree expansion of geopotential U is given by

$$U\left(R,\tilde{\Theta}\right) = \frac{GM}{R}\left[1-\left(\frac{\rho}{R}\right)^2 J_2 \frac{3\sin^2\tilde{\Theta}-1}{2}\right] \qquad (10)$$

where GM is the gravitational constant times the mass of the earth, R is the distance from the center of the earth, ρ is the radius of the earth, $\tilde{\Theta}$ is geocentric latitude, and $J_2=1.0826\times10^{-3}$ is the non-dimensional coefficient that characterizes the difference between the polar and equatorial radii. The flattening of the earth represented by J_2 is the largest perturbing effect, being three orders of magnitude larger than any other perturbing force. Using (10), the time rates of change of the longitude of the ascending node Ω and the angle of perigee ω are then given by

$$\frac{d\Omega}{dt} = -\frac{3}{2}\frac{1}{\left(1-\varepsilon^2\right)^2}\sqrt{\frac{GM}{a^3}}\left(\frac{\rho}{a}\right)^2 J_2 \cos\alpha \qquad (11a)$$

$$\frac{d\omega}{dt} = \frac{3}{4} \frac{1}{\left(1-\varepsilon^2\right)^2} \sqrt{\frac{GM}{a^3}} \left(\frac{r_e}{a}\right)^2 J_2\left(5\cos^2\alpha - 1\right) \tag{11b}$$

where ε is the eccentricity, a is the major semi-axis, and α is the inclination angle. The quantity $d\Omega/dt$ is called the nodal precession and $d\omega/dt$ is called the apsidal precession. Referencing Figure 2A, the nodal precession is the rotation of the orbital plane about the polar axis, and the apsidal precession is the rotation of the whole orbit in the orbital plane. When the nodal precession rate is equal to the angular speed of the earth around the sun, the orbit is said to be sun-synchronous. The SSM/I series specifically use this property to achieve constant local time of observation. Using nominal SSM/I values of $\varepsilon = 0.001$, $a = 7220$ km, and $\alpha = 98.8°$ gives a nodal precession rate of 0.986°/day, which is the same as the angular speed of the earth around the sun. Since the apsidal precession rate is the rotation of the whole orbit in the orbital plane, in the SSM/I data it appears as a precession of the perigee (or apogee) in latitude. The nominal SSM/I values give an apsidal precession rate of 2.85°/day, or a period of 126.5 days. This period can be estimated from SSM/I data by constructing a time series of the perigee angle, which is given by the orbit position of the minimum altitude anomaly. The anomaly is defined as the altitude minus the mean altitude versus orbit position. The perigee angle (not shown) is a saw-tooth curve in time, and finding the period gives an average of 125 days for all the SSM/I satellites. *Colton and Poe* [1999] give values ranging from 120 to 129 days.

The altitude anomaly as a function of orbit position is a family of cosine curves with phases given by the perigee angle. Thus for simplicity, Figure 4C shows the EIA minus the orbit position average (Fig. 4B) plotted versus the orbit position minus the perigee angle. Each satellite has a curve with a cosine shape and amplitude given in Table 1. The amplitudes are comparable to the mean variability shown in Figure 4B, except for F10 which experienced a

much larger perigee effect. Thus, synthesizing all of the above discussion, variability in the scan-average EIA is accurately described by

$$\theta = \overline{\theta}\left(month\right) + \overline{\theta}\left(\psi_{orb}\right) - \alpha_{per}\cos\left(\psi_{orb} - \psi_{per}\right) \tag{12}$$

where $\overline{\theta}\left(month\right)$ is the monthly global average EIA (Fig. 3B) smoothed with a low-pass filter with a width of one year to isolate the long-term trends, $\overline{\theta}\left(\psi_{orb}\right)$ is the mean EIA anomaly versus orbit position ψ_{orb} (Fig. 4B), α_{per} is the EIA perigee anomaly amplitude (Table 1), and ψ_{per} is the perigee angle. The EIA predicted by (12) is compared against the measured EIA in the SSM/I dataset in Figure 4D. More than 99% of the observations have differences less than 0.01°, except for F10 for which more than 99% of the observations have differences less than 0.04°.   The histograms predicted by (12) are visually indistinguishable from the actual histograms in Figure 3A. Thus, despite its simplicity, (12) explains the shoulders and multi-modal tendencies of the observed EIA histograms. Please note that (12) is not used in SSM/I processing; it is provided here to quantitatively describe the interaction of the orbital and perigee modes of EIA variability.

5. Radiative Transfer Model

We calculate estimates of the change in brightness temperature with respect to earth incidence angle $\partial T_B / \partial \theta$ using a standard centered difference formula

$$\frac{\partial T_B}{\partial \theta} = \frac{T_B\left(\theta + \Delta\theta; f, p, T_S, W, \phi_r, V, L\right) - T_B\left(\theta - \Delta\theta; f, p, T_S, W, \phi_r, V, L\right)}{2\Delta\theta} \tag{13}$$

with $\Delta\theta = 0.01°$. The values of T_B are provided by the RSS radiative transfer model (RTM), and depend on frequency f, polarization p, sea surface temperature T_S, surface wind speed W, wind direction relative to the azimuth angle ϕ_r, columnar water vapor V, and columnar cloud liquid water L. The RSS RTM is the product of over 35 years of development, usage, and testing [*Wentz*, 1975, 1976, 1978, 1983, 1997; *Wentz and Spencer*, 1998; *Wentz and Meissner*, 2000; *Meissner and Wentz*, 2002; *Meissner and Wentz*, 2003; *Meissner and Wentz*, 2004; *Meissner and Wentz*, 2006; *Hilburn and Wentz*, 2008a]. This section describes the RTM and shows the dependence of $\partial T_B / \partial \theta$ on scene parameters.

The T_B at the top of the atmosphere as seen by a satellite radiometer is the sum of three parts: upwelling atmospheric radiation, emission from the sea surface that is attenuated by the intervening atmosphere, and downwelling atmospheric radiation that is reflected upward by the sea surface and attenuated by the intervening atmosphere. This can be expressed as

$$T_B\left(f, p, \theta, T_S, W, \phi_r, V, L\right) = T_{BU} + \tau E T_S + \tau\left(1 - E\right)\left[T_{BD} + \tau T_{BC} + S\right] \tag{14}$$

where T_{BU} and T_{BD} are the upwelling and downwelling atmospheric brightness temperatures, τ is the atmospheric transmittance, E is the sea-surface emissivity, T_S is the surface temperature, T_{BC} is the cosmic background radiation temperature (2.7 K), and S accounts for non-specular surface scattering of downwelling atmospheric radiation from other parts of the sky into the satellite viewing path. The model does not include atmospheric scattering, so its intended

application is outside of rain, where atmospheric scattering is negligible. This closed-form expression is a highly accurate approximation to the full integral form of the radiative transfer equation [*Wentz* 1983] that allows for rapid calculation of brightness temperatures.

Focusing first on the atmospheric terms (T_{BU}, T_{BD} and τ), the upwelling and downwelling brightness temperatures are given by

$$T_{BU} = T_U \left(1 - \tau\right) \tag{15a}$$

$$T_{BD} = T_D \left(1 - \tau\right) \tag{15b}$$

where T_U and T_D are the upwelling and downwelling effective air temperatures. In the RTM, the effective air temperatures depend primarily on water vapor [*Wentz*, 1997; *Wentz and Meissner*, 2000]. The atmospheric transmittance τ is the sum of absorption from oxygen A_O, water vapor A_V, and liquid water A_L

$$\tau = \exp\left[-\sec\theta\left(A_O + A_V + A_L\right)\right] \tag{16}$$

Oxygen absorption is based on the model of *Rosenkranz* [1998]. The vapor absorption model is based on *Wentz and Meissner* [2000], but recent changes were made to increase the foreign-broadened continuum and to decrease the self-broadened continuum [*Meissner*, personal communication]. These changes were motivated by an analysis of WindSat and SSM/I T_B in which the 0.008 mm clear sky bias in Version-6 cloud water retrievals was removed [*Horváth and Gentemann*, 2007]. The new continuum model is very close to the latest version of MonoRTM [*Payne et al.*, in preparation]. Liquid water absorption is modeled as a linear function of vertically integrated liquid water, and depends on the temperature of the water droplets [*Wentz*, 1997; *Wentz and Meissner*, 2000].

As for the atmosphere, the dependence of T_B on EIA is due to the path through the atmosphere. Increasing either the EIA or the absorption will cause the transmittance to decrease

and the upwelling and downwelling T_B to increase, because the satellite is viewing a longer or more opaque path through the atmosphere. Thus, both the transmittance (τ) and the change in transmittance with EIA ($\partial\tau/\partial\theta$) are decreasing with vapor (Fig. 5A,B); while both the upwelling and downwelling brightness temperatures (T_{BU} and T_{BD}) and their change with EIA ($\partial T_{BU}/\partial\theta$ and $\partial T_{BD}/\partial\theta$) are increasing with vapor (Fig. 5A,B). For the purpose of illustrating the RTM, Figs. 5 and 6 were constructed assuming an EIA of 53.25º, a relative wind direction of 0º, no cloud water, and a typical sea surface temperature for a given vapor amount ($T_S = 0.8337\,V - 3.029\text{E}^{-5}\,V^{3.33}$ for $V \leq 48$ mm and $T_S = 28°C$ for $V > 48$ mm).

Focusing next on the surface, the sea surface emissivity E is the sum of three components

$$E = E_0 + E_W + E_\phi \tag{17}$$

where E_0 is the specular emissivity, E_W is the component of emissivity due to wind-induced surface roughening, and E_ϕ is the component of emissivity that depends on the angle between the azimuth angle and the wind direction. The wind direction component E_ϕ has almost no effect on $\partial T_B/\partial\theta$ and will not be discussed here, but *Meissner and Wentz* [2002] provides a detailed discussion.

The specular emissivity is the part of the emissivity that accounts for a flat ocean surface not roughened by wind. The specular emissivity for vertical E_{0V} and horizontal E_{0H} polarizations are given by the Fresnel equations:

$$E_{0V} = 1 - \left| \frac{\varepsilon\cos(\theta) - \sqrt{\varepsilon - \sin^2(\theta)}}{\varepsilon\cos(\theta) + \sqrt{\varepsilon - \sin^2(\theta)}} \right|^2 \tag{18a}$$

$$E_{0H} = 1 - \left| \frac{\cos(\theta) - \sqrt{\varepsilon - \sin^2(\theta)}}{\cos(\theta) + \sqrt{\varepsilon - \sin^2(\theta)}} \right|^2 \tag{18b}$$

where ε is the complex dielectric constant of water. The dielectric constant is a function of frequency, water temperature, and salinity and is given in *Meissner and Wentz* [2004]. From these equations come the familiar result that E_{0V} is very close to twice E_{0H} for SSM/I EIAs and frequencies (Fig. 5C). These equations also provide the crucial information that E_{0V} increases with EIA, but E_{0H} decreases with EIA (Fig. 5D). This difference between vertical and horizontal polarization emissivity is key to understanding the differences in $\partial T_B / \partial \theta$ between the two polarizations.

Wind roughening of the ocean surface causes the emission to increase and become less polarized at SSM/I EIAs (Fig. 5C). *Wentz and Meissner* [2000] describe how the wind induced emissivity is modeled; which includes polarization mixing by waves longer than the radiation wavelength (about 1 cm), diffraction by shorter waves, and an increase in emissivity due to the effects of sea foam. For our purposes, it is important to note that when the wind-induced component is added, $\partial E_V / \partial \theta$ and $\partial E_H / \partial \theta$ have the same signs as the specular values, but the magnitudes both decrease so that $\partial E_V / \partial \theta$ decreases with wind speed and $\partial E_H / \partial \theta$ increases with wind speed (Fig. 5D).

Finally, the nonspecular scattering of downwelling atmospheric radiation S couples the surface and the atmosphere. Most of the reflected downwelling radiation viewed by the sensor will be from the zenith angle equal to the EIA. This specular reflection is given by $(1-E)\,T_{BD}$. Since the surface is also roughened by wind, radiation from other parts of the sky will also be reflected into the viewing direction of the sensor, increasing the amount of reflected downwelling radiation. This effect is modeled using the same sea surface model as used for wind-induced emissivity [*Wentz and Meissner*, 2000]. S depends on the wind speed and atmospheric transmittance, as well as frequency and EIA. Figure 5E shows that S_H is about four

times larger than S_V. Figure 5E also shows that S increases with wind speed up to 10 ms^{-1}, but then decreases slightly at higher wind speeds. S increases with vapor, except for 22 GHz at vapor amounts greater than 30 mm, because as the absorption increases and the atmosphere becomes more opaque, the sky radiation becomes more isotropic. $\partial S/\partial\theta$ is generally negative, indicating that as the EIA increases, less radiation from other parts of the sky is reflected into the satellite viewing direction (Fig. 5F).

Figure 6 shows how the different components in the RTM affect $\partial T_B/\partial\theta$ and vary with water vapor and wind speed. The leftmost column of Figure 6 shows $\partial T_B/\partial\theta$ with just the specular emissivity ($E = E_0$) and without the S term. Since this uses the specular emissivity, there is no dependence of $\partial T_B/\partial\theta$ on wind speed, but it does depend on water vapor. For v-pol at 19 and 37 GHz, $\partial T_B/\partial\theta$ is relatively constant with respect to water vapor with a value around 2.2-2.4 K/deg. At 22 GHz, $\partial T_B/\partial\theta$ is positive but decreases with vapor from 2.4 to 1.2 K/deg. For h-pol, $\partial T_B/\partial\theta$ is negative at low vapor with a value around -1 K/deg and increases with vapor to a value around 0.6 K/deg at high vapor. To understand this behavior, note that change in attenuated surface emission ($\partial(\tau E T_S)/\partial\theta$) is a combination of two effects: a change in transmittance ($E T_S\,\partial\tau/\partial\theta$) and a change in emissivity ($\tau T_S\,\partial E/\partial\theta$). These effects are both decreasing with vapor for v-pol and reinforce each other; but cancel each other for h-pol. Since the change in upwelling radiation ($\partial T_{BU}/\partial\theta$) is increasing with vapor, when combined with the change in attenuated surface emission, the change in upwelling radiation dominates for h-pol, but cancels for v-pol. For 22V, the decrease in attenuated surface emission is strong enough that in combination with the change in reflected and attenuated downwelling radiation, which is also decreasing with vapor, $\partial T_B/\partial\theta$ decreases with vapor.

25

The second column of Figure 6 shows $\partial T_B / \partial \theta$ when the wind-induced emissivity is included, i.e. $E = E_0 + E_W$. Comparing the first and second columns of Figure 6, the effect of the wind-induced emissivity can be seen. It causes $\partial T_B / \partial \theta$ to decrease with wind speed for v-pol from 2.4 to 1.5 K/deg, but it has little effect on $\partial T_B / \partial \theta$ for h-pol. This is because the two effects contributing to the change in attenuated surface emission ($\partial(\tau E T_S)/\partial \theta$) are both decreasing with wind speed for v-pol, but balance each other for h-pol.

The third column of Figure 6 shows how the nonspecular scattering of downwelling radiation S affects $\partial T_B / \partial \theta$. It reduces $\partial T_B / \partial \theta$ somewhat for v-pol at higher wind speeds. For h-pol it changes how $\partial T_B / \partial \theta$ varies with wind speed. The shape of S in Figure 5E is clearly impressed on the h-pol plots in the third column of Figure 6, and since S is much smaller for v-pol, it makes a much smaller effect on $\partial T_B / \partial \theta$. The remaining rightmost two columns of Figure 6 will be discussed in Section 6.

6. Earth Incidence Angle Normalization Algorithm and Error Analysis

The adjustment for incidence angle uses the Taylor series (2) with a nominal incidence angle of 53.25°, which is roughly the mean incidence angle for all SSM/I. The derivative is specified by

$$\frac{\partial T_B}{\partial \theta}[f,p] = a_0 + \sum_{i=1}^{5} a_i (T_{Bi} - 150) + \sum_{i=1}^{5} a_{(i+5)} (T_{Bi} - 150)^2 + \sum_{i=1}^{5} a_{(i+10)} \ln(290 - T_{Bi}) \quad (19)$$

where T_{Bi} for $i=1,5$ are the 19V, 19H, 22V, 37V, and 37H brightness temperatures in that order. The coefficients a_0 to a_{15} are given in Table 2. While good results can be obtained with just the linear terms, we found the nonlinear terms did improve the fit. The coefficients in (19) were derived using multiple linear regression. All SSM/I observations (F08-F15) for the entire period 1987-2009 were used for the regression. Each observation was weighted equally, so the adjustment is optimized for typical meteorological and oceanographic conditions. Land and ice-covered surfaces were excluded using land and sea-ice masks and rain was excluded using SSM/I rain rate retrievals. The input variables for the regression are the SSM/I brightness temperatures. The T_B were constrained to be less than 280 K to avoid singularities in the logarithm, however inspection of global ocean rain-free brightness temperatures for all SSM/I showed that T_B were never greater than 270 K. Since only v-pol antenna temperatures are available at 22 GHz, we used

$$T_{B22V} = 1.01993 T_{A22V} + 1.994 \quad (20)$$

to specify T_B [*Wentz*, 1991]. The measured variable $\partial T_B / \partial \theta$ is specified by (13) using the RSS RTM. The RTM requires wind speed, columnar water vapor, and columnar cloud liquid water; which were specified using RSS SSM/I geophysical retrievals. If SSM/I geophysical retrievals were not available for any reason, that observation was not included in the regression. Sea

surface temperature was specified using Reynolds V2 OI SST, and wind direction was specified using NCEP GDAS surface wind direction.

Errors in the regression (19) can be determined by comparing the "raw" unadjusted T_B and the "regression" adjusted T_B against the T_B adjusted using the "exact" adjustment provided by the RTM using (13). Table 3 shows that the bias in raw v-pol T_B is between -0.15 to -0.18 K. The standard deviations for raw-exact v-pol T_B differences are between 0.40 to 0.47 K. The h-pol T_B have much smaller biases, and the standard deviations are near 0.1 K. Using the regression to adjust T_B lowers the biases to less than the 0.005 K level for all channels, and the standard deviations are all less than 0.16 K. Focusing on W_B calculated by (1), the raw-exact W_B differences have a standard deviation of 0.225 mm, and the regression lowers this to 0.004 mm. Figure 7 shows errors in W_B as a function of scene parameters. Figures 7A and 7C show that raw W_B have a negative bias that increases with increasing SST and vapor. The tight envelope on raw W_B in Figure 7E shows, beyond any doubt, that incidence angle is the cause of the errors in W_B. The regression-adjusted W_B have extremely tight envelopes, demonstrating that the correction (19) with coefficients in Table 2 performs very well in all conditions. The only conditions in which the standard deviation envelope of the regression-adjusted W_B is visually discernable in Figure 7 are for wind speeds greater than 20 ms^{-1}, and for water vapor values less than 5 mm or greater than 60 mm. Wind speeds greater than 20 ms^{-1} occur 0.7% of the time. Water vapor values less than 5 mm occur 2.4% of the time, and water vapor values greater than 60 mm occur 0.6% of the time.

The spurious trend in W_B removed by the adjustment is shown in Figure 7F. The regression does an extremely good job at removing the spurious trend. A more detailed examination of trends is given in Figure 8 and Table 4. Since the global average $\partial T_B / \partial \theta$ for h-pol is around

zero, the trends for h-pol T_B change very little when adjusted for incidence angle. The v-pol values change dramatically. The raw v-pol time series (Fig. 8A, 8C, and 8E) have large intersatellite offsets and negative trends around -0.3 to -0.4 K/decade. The regression removes the intersatellite offsets and increases the trends to near zero. The negative trends and large intersatellite offsets are very noticeable for W_B (Fig. 8F) and mimic the incidence angle time series in Figure 3B. Application of the regression removes the offsets and increases the trend from -0.227 K/decade (-4.4%/decade) for the raw time series to -0.068 K/decade (-1.3%/decade) for the adjusted time series. The regression reproduces the exact trends to within 0.0003 K/decade for 19 and 22 GHz T_B, within 0.0008 K/decade for 37 GHz T_B, and better than 0.0001 mm for W_B. The adjustment does not produce large changes in the overall mean T_B and W_B (Table 4). While the incidence angle normalization properly and considerably reduced the magnitude of the W_B trend; the new W_B still shows a decreasing trend, yet with much smaller magnitude. The decreasing W_B trend is due to equal contributions from the decreasing 19V trend and the increasing 19H trend times the coefficients in Equation (1). Since W_B is reasonably correlated with total water vapor, and since total water vapor is known to have a small positive trend, we have concerns about the current W_B-T_B retrieval algorithm, and further research and validation would be needed before a definitive statement of W_B trend accuracy can be made.

The fourth column of Figure 6 shows the regression versus wind and vapor. It can be compared against the third column of Figure 6 to see how it compares against the exact values from the RTM. The regression performs very well overall. At high wind speeds for v-pol the regression values for $\partial T_B / \partial \theta$ are slightly larger than the exact values. The regression is not able to fully reproduce the effect of the nonspecular scattering term in the RTM because of its detailed structure in wind speed, especially at high vapor values. The fifth column of Figure 6

shows the adjustment of *Fuhrhop and Simmer* [1996]. There is a basic similarity to our correction, although the slopes of constant $\partial T_B/\partial\theta$ lines in wind speed and water vapor space do exhibit prominent differences, especially for h-pol. Given that the *Fuhrhop and Simmer* [1996] correction was based on a different RTM, these differences are not surprising. Since the adjustment derived in this paper was based on the RSS RTM, it does a better job of reproducing its structure than does the *Fuhrhop and Simmer* [1996] adjustment.

7. Conclusions

This paper describes earth incidence angle (EIA) trends and variability in the SSM/I dataset and their effect on brightness temperatures. The Goddard Satellite-based Surface Turbulent Fluxes (GSSTF) dataset uses RSS Version-6 SSM/I brightness temperatures to derive the bottom layer water vapor W_B, which is used in the calculation of latent heat flux. While RSS has always handled EIA variations using retrieval algorithms parameterized in terms of EIA, legacy algorithms that do not account for EIA variations will have large intersatellite offsets and spurious long-term trends. The change in T_B with EIA for h-pol is about 0 K/deg on average. Thus EIA effects are not evident on global time series of h-pol T_B. For v-pol, the change in T_B with EIA is about 2 K/deg, and failure to account for EIA will produce spurious trends in v-pol T_B on the order of -0.3 K/decade. The change in T_B with EIA is not constant, but varies with the meteorological conditions in the satellite footprint. For v-pol, $\partial T_B / \partial \theta$ decreases with wind speed and is relatively constant with vapor. However, for h-pol, $\partial T_B / \partial \theta$ varies more strongly with vapor than with wind. These differences are due to differences in v-pol and h-pol sea surface emissivity. Section 5 details the subtle cancelations between different physical effects that produce these different overall responses.

Section 3 explained how EIA is calculated, and Section 4 characterized the variability of EIA in the SSM/I dataset. The main source of variability is due to changes in altitude as the satellite makes an orbit. This variability is modulated on four month time scales by the precession of the perigee. Section 4 described this in detail and provided a mathematical model to summarize EIA variability. The RSS radiative transfer model (RTM) was described in Section 5, and the EIA-dependent parts were examined. In order to use legacy algorithms that do not include EIA dependence, the RSS RTM was used to derive an algorithm that normalizes T_B to a common

31

nominal EIA. This is the same RTM that was used to calibrate RSS SSM/I data. The algorithm

was presented in Section 6, and its accuracy relative to the RTM was characterized. Validation

of $\partial T_B / \partial \theta$ would require specialized observational data, and we encourage measurement efforts

to better quantify $\partial T_B / \partial \theta$ over all surface types and in all meteorological conditions. The

algorithm performs very well relative to the RTM in all meteorological conditions. Trends

calculated from the regression-adjusted T_B agree very well with trends calculated with an exact

adjustment from the RTM. The adjustment increases the W_B trends by 0.16 mm/decade or

3.1%/decade. This adjustment will be implemented in a future version of GSSTF, the results of

which will be described by *Shie et al*. in a separate paper.

Appendix: Coordinate transformation and range distance calculation

Given the satellite position vector $\mathbf{R}_{(e)}$ and velocity vector $\mathbf{V}_{(e)}$ in geocentric coordinates, and defining

$$\mathbf{Q}_{(e)} = \frac{\mathbf{V}_{(e)} \times \mathbf{R}_{(e)}}{\left| \mathbf{V}_{(e)} \times \mathbf{R}_{(e)} \right|} \tag{A1a}$$

and

$$R_1 \mathbf{e}_1 + R_2 \mathbf{e}_2 + R_3 \mathbf{e}_3 = \frac{\mathbf{R}_{(e)}}{\left| \mathbf{R}_{(e)} \right|} \tag{A1b}$$

then the coefficients of the transformation matrix (5) are given by

$$\mathbf{Z}_{(e)} = \frac{-R_1 \mathbf{e}_1 - R_2 \mathbf{e}_2 - R_3 \left(\dfrac{1+\Delta}{f+\Delta} \right) \mathbf{e}_3}{\sqrt{R_1^2 + R_2^2 + R_3^2 \left(\dfrac{1+\Delta}{f+\Delta} \right)^2}} \tag{A1c}$$

$$\mathbf{X}_{(e)} = \frac{\mathbf{Q}_{(e)} \times \mathbf{Z}_{(e)}}{\left| \mathbf{Q}_{(e)} \times \mathbf{Z}_{(e)} \right|} \tag{A1d}$$

$$\mathbf{Y}_{(e)} = \frac{\mathbf{Z}_{(e)} \times \mathbf{X}_{(e)}}{\left| \mathbf{Z}_{(e)} \times \mathbf{X}_{(e)} \right|} \tag{A1e}$$

where $f = \left(\rho_p / \rho_e \right)^2$ and

$$\Delta = \left(\frac{R-\rho}{\rho_e} \right) \sqrt{1 - \frac{(1-f)\sin^2 \tilde{\Theta}_S}{f^2 \cos^2 \tilde{\Theta}_S + \sin^2 \tilde{\Theta}_S}} \tag{A1f}$$

$$\rho = \frac{\rho_p}{\sqrt{f \cos^2 \tilde{\Theta}_S + \sin^2 \tilde{\Theta}_S}} \tag{A1g}$$

where $R = |\mathbf{R}_{(e)}|$ and is the $\tilde{\Theta}_S$ geocentric latitude of the satellite. The geocentric latitude of the satellite $\tilde{\Theta}_S$ is the angle between the equatorial plane and a line from E to S (Fig. 2A). Thus,

$\sin(\tilde{\Theta}_S) = R_3$ and $\cos(\tilde{\Theta}_S) = \sqrt{R_1^2 + R_2^2}$.

The range distance from the satellite to the earth r in (6) is given by

$$r = R\left(\frac{b - \sqrt{b^2 - ac}}{a}\right) \tag{A2a}$$

where

$$a = 1 + \delta B_3^2 \tag{A2b}$$

$$b = -R_1 B_1 - R_2 B_2 - R_3 B_3 - \delta R_3 B_3 \tag{A2c}$$

$$c = 1 - \left(\frac{\rho_e}{R}\right)^2 + \delta R_3^2 \tag{A2d}$$

where B_1, B_2, and B_3 are given by (5) and $\delta = f^{-1} - 1$. Note that if the argument $b^2 - ac$ is less than zero, then the boresight vector does not intercept the earth.

References

Capderou, M. (2005), *Satellites: Orbits and missions*. Springer, Paris.

Chelton, D. B., and F. J. Wentz (2005), Global microwave satellite observations of sea surface temperature for numerical weather prediction and climate research, *Bulletin of the American Meteorological Society*, 86, 1097-1115.

Chiu, L. S., R. Chokngamwong, Y. Xing, R. Yang, and C.-L. Shie (2008), "Trends" and variations of global oceanic evaporation datasets from remote sensing, *Acta Oceanologica Sinica*, **27**, 124-135.

Chou, S.-H., R. M. Atlas, C-L. Shie and J. Ardizzone (1995), Estimates of surface humidity and latent heat fluxes over oceans from SSM/I data, *Monthly Weather Review*, 123, 2405-2425.

Chou, S.-H., C.-L. Shie, R. M. Atlas, and J. Ardizzone (1997), Air-sea Fluxes Retrieved from Special Sensor Microwave Imager Data, *Journal of Geophysical Research*, 102, 12705-12726.

Chou, S.-H., E. Nelkin, J. Ardizzone, R. M. Atlas, and C-L. Shie (2003), Surface turbulent heat and momentum fluxes over global oceans based on the Goddard satellite retrieval, version 2 (GSSTF2), *Journal of Climate*, 16, 3256-3273.

Colton, M. C., and G. A. Poe (1999), Intersensor calibration of DMSP SSM/I's: F-8 to F-14, 1987-1997, *IEEE Transactions on Geoscience and Remote Sensing*, 37, 418-439.

Fuhrhop, R., and C. Simmer (1996), SSM/I brightness temperature corrections for incidence angle variations, *Journal of Atmospheric and Oceanic Technology*, 13, 246-254.

Gentemann, C. L., T. Meissner, and F. J. Wentz (2010), Accuracy of satellite sea surface temperatures at 7 and 11 GHz, *IEEE Transactions on Geoscience and Remote Sensing*, 48, 1009-1018.

Hollinger, J. P., J. L. Peirce, and G. A. Poe (1990), SSM/I instrument evaluation, *IEEE Transactions on Geoscience and Remote Sensing*, 28, 781-790.

Horváth, Á., and C. L. Gentemann (2007), Cloud-fraction-dependent bias in satellite liquid water path retrievals of shallow, non-precipitating marine clouds, *Geophysical Research Letters*, 34, L22806, doi:10.1029/2007GL030625.

Hilburn, K. A., and F. J. Wentz (2008a), Intercalibrated passive microwave rain products from the unified microwave ocean retrieval algorithm (UMORA), *Journal of Applied Meteorology and Climatology*, 47, 778-794.

Hilburn, K. A., and F. J. Wentz (2008b) Mitigating the impact of RADCAL beacon contamination on F15 SSM/I ocean retrievals, *Geophysical Research Letters*, 35, L18806, doi:10.1029/2008GL034914.

Mears, C. A., M. C. Schabel, and F. J. Wentz (2003), A reanalysis of the MSU channel 2 tropospheric temperature record, *Journal of Climate*, 16, 3650-3664.

Meissner, T., and F. J. Wentz (2002), An updated analysis of the ocean surface wind direction signal in passive microwave brightness temperatures, *IEEE Transactions on Geoscience and Remote Sensing*, 40, 1230-1240.

Meissner, T., and F. J. Wentz (2003), A radiative transfer model function for 85.5 GHz Special Sensor Microwave Imager ocean brightness temperatures, *Radio Science*, 38, 8066, doi:10.1029/2002RS002655.

Meissner, T., and F. J. Wentz (2004), The complex dielectric constant of pure and sea water from microwave satellite observations, *IEEE Transactions on Geoscience and Remote Sensing*, 42, 1836-1849.

Meissner, T., and F. J. Wentz (2006), Polarization rotation and the third stokes parameter: The effects of spacecraft attitude and faraday rotation, *IEEE Transactions on Geoscience and Remote Sensing*, 44, 506-515.

Reynolds, R. W., N. A. Rayner, T. M. Smith, D. C. Stokes, and W. Wang (2002), An improved in situ and satellite SST analysis for climate. *J. Climate*, 15, 1609–1625.

Rosenkranz, P. (1998), Water vapor microwave continuum absorption: A comparison of measurements and models, *Radio Science*, 33, 919-928.

Schulz J., P. Schluessel, and H. Grassl (1993), Water vapor in the atmospheric boundary layer over oceans from SSM/I measurements, *Int. J. Remote Sens.*, 14, 2773–2789.

Shie, C.-L., L. S. Chiu, R. Adler, P. Xie, I-I Lin, F.-C. Wang, E. Nelkin, R. Chokngamwong, W. S. Olson, and D. A. Chu (2009), A note on reviving the Goddard Satellite-based Surface Turbulent Fluxes (GSSTF) dataset, *Advances in Atmospheric Sciences*, 26(6), 1071-1080.

Shie, C.-L., L. S. Chiu, R. Adler, I-I Lin, E. Nelkin, and J. Ardizzone (2010), The Goddard Satellite-Based Surface Turbulent Fluxes Dataset --- Version 2b (GSSTF 2b). Distributed via NASA GES DISC in October 2010.

Shie, C.-L., (2010a), Science background for the reprocessing and Goddard Satellite-based Surface Turbulent Fluxes (GSSTF2b) Data Set for Global Water and Energy Cycle Research. Science Document for the Distributed GSSTF2b via Goddard Earth Sciences (GES) Data and Information Services Center (DISC), 18 pp. (Available online: http://disc.sci.gsfc.nasa.gov/measures/documentation/Science-of-the-data.pdf)

Shie, C.-L., (2010b), A recently revived dataset of satellite-based global air-sea surface turbulent fluxes (GSSTF2b) – features and applications, paper presented at 17th AMS Conference on

Satellite Meteorology and Oceanography, Annapolis, MD. (Available online: http://disc.sci.gsfc.nasa.gov/measures/documentation/2010-Sat-Air-Sea-Shie.pdf)

Shie, C.-L., and K. Hilburn (2011), A newly revived satellite-based global air-sea surface turbulent fluxes dataset and its dependence on the SSM/I brightness temperature, 2011 IEEE IGARSS, Vancouver, Canada, 25-29 July. Extended Abstract (4 pp), *Proceedings* (published in CD).

Wentz, F. J. (1975), A two-scale scattering model for foam-free sea microwave brightness temperatures, *Journal of Geophysical Research*, 80, 3441-3446.

Wentz, F. J. (1976), Cox and Munk's sea surface slope variance, *Journal of Geophysical Research*, 81, 1607-1608.

Wentz, F. J. (1978), The forward scattering of microwave solar radiation from a water surface, *Radio Science*, 13, 131-138.

Wentz, F. J. (1983), A model function for ocean microwave brightness temperatures, *Journal of Geophysical Research*, 88, 1892-1908.

Wentz, F. J. (1997), A well calibrated ocean algorithm for special sensor microwave / imager, *Journal of Geophysical Research*, 102, 8703-8718.

Wentz, F. J., and M. C. Schabel (1998), Effects of satellite orbital decay on MSU lower tropospheric temperature trends, *Nature*, 394, 661-664.

Wentz, F. J., and R. W. Spencer (1998), SSM/I rain retrievals within a unified all-weather ocean algorithm, *Journal of the Atmospheric Sciences*, 55, 1613-1627.

Wentz, F. J., L. Ricciardulli, K. A. Hilburn, and C. A. Mears (2007), How much more rain will global warming bring?, *Science*, 317, 233-235.

Wentz, F. J. (1993), User's Manual: SSM/I Antenna Temperature Tapes (Revision 2), report number 120193, Remote Sensing Systems, Santa Rosa, CA, 36 pp. (available online: http://www.remss.com/papers/ssmi/TA/SSMI_TA_manual_rev_2.pdf)

Wentz, F. J. (1991), User's Manual: SSM/I Antenna Temperature Tapes (Revision 1), report number 120191, Remote Sensing Systems, Santa Rosa, CA, 73 pp. (available online: http://www.remss.com/papers/ssmi/TA/ssmi_TA_manual_rev_1.pdf)

Wentz, F. J., and T. Meissner (2000), AMSR Ocean Algorithm, Version 2, report number 121599A-1, Remote Sensing Systems, Santa Rosa, CA, 66 pp. (available online: http://www.remss.com/papers/amsr/AMSR_Ocean_Algorithm_Version_2.pdf)

Wilheit, T. T., and A. T. C. Chang (1980), An algorithm for retrieval of ocean surface and atmospheric parameters from the observations of the scanning multichannel microwave radiometer, *Radio Science*, 15, 524-544.

Satellite	Dates	Mean EIA (deg)	EIA Trend (deg/dec)	Altitude (km)	θ_n (deg)	ω_n (deg)	α_{per} (deg)
F08	Jul 1987-Dec 1991	53.36	-0.1855	858.7	45.00	-129.60	0.1128
F10	Dec 1990-Nov 1997	53.18	-0.0914	796.5	45.37	51.10	0.6075
F11	Dec 1991-May 2000	53.32	-0.0391	857.8	44.98	51.05	0.0984
F13	May 1995-Nov 2009	53.08	-0.0744	857.5	44.80	50.90	0.0544
F14	May 1997-Aug 2008	53.29	-0.0861	856.4	44.97	50.35	0.0681
F15	Dec 1999-Aug 2006	52.94	-0.0913	852.2	44.74	51.20	0.0769

Table 1. List of SSM/I sensors with dates of operation, mean earth incidence angle, the trend in earth incidence angle, mean altitude, boresight nadir angle θ_n, boresight azimuth angle ω_n, and perigee amplitude coefficient α_{per}.

Coefficient	19V	19H	22V	37V	37H
a_0	-3.803320E+01	-2.935334E+01	2.671031E+01	-8.232317E+01	-3.424210E+01
a_1	1.248196E-01	5.702329E-02	7.362724E-02	1.472073E-01	8.759297E-02
a_2	-1.152058E-01	-9.407873E-02	-1.526919E-01	-5.880490E-02	-1.051417E-01
a_3	1.899037E-02	3.452298E-02	2.690668E-02	2.844496E-02	3.349962E-02
a_4	-3.929251E-02	-1.387860E-01	1.056787E-02	-2.876937E-02	-1.366640E-01
a_5	5.121212E-02	1.470717E-01	-1.794357E-02	-6.046791E-03	1.109226E-01
a_6	8.987391E-04	-1.393160E-04	5.862015E-04	1.195428E-03	-6.309741E-04
a_7	-1.916061E-04	4.894893E-05	-3.166680E-04	-5.090897E-08	2.361817E-04
a_8	-9.560483E-05	4.218291E-06	2.198816E-05	-2.210936E-04	-7.014447E-05
a_9	-2.315692E-05	5.670663E-04	2.747827E-04	3.859362E-04	1.647330E-03
a_{10}	9.485205E-05	7.572780E-05	-7.660942E-05	-8.639943E-05	-2.701170E-04
a_{11}	1.991876E+01	6.024204E+00	1.223296E+01	2.478794E+01	4.244867E+00
a_{12}	-1.532517E+01	-1.351231E+01	-2.008207E+01	-8.387952E+00	-1.299293E+01
a_{13}	-3.896642E-01	1.959212E-01	1.780794E+00	-1.030973E+00	-5.056202E-01
a_{14}	-6.418455E+00	-5.662755E+00	3.078366E-01	-2.456300E+00	3.508040E+00
a_{15}	9.903399E+00	1.899347E+01	2.911536E-01	3.699573E+00	1.270627E+01

Table 2. Coefficients for regression. See (19) and accompanying text for the terms associated with each coefficient.

Channel	Bias		Standard Deviation	
	Raw	Regression	Raw	Regression
19V	-0.1775	-0.0022	0.4679	0.0098
19H	0.0053	-0.0009	0.0971	0.0100
22V	-0.1502	-0.0029	0.4095	0.0103
37V	-0.1617	-0.0042	0.4203	0.0142
37H	-0.0024	-0.0036	0.0688	0.0152
W_B	-0.0805	-0.0008	0.2246	0.0043

Table 3. Bias and standard deviation for the raw (no adjustment) and the regression-adjusted T_B (K) and W_B (mm) versus the exact values specified using the RTM.

Channel	Means			Trends		
	Raw	Regression	Exact	Raw	Regression	Exact
19V	194.65	194.81	194.82	-0.4302	-0.0952	-0.0954
19H	130.03	130.03	130.03	0.1786	0.1471	0.1468
22V	219.75	219.88	219.89	-0.3004	-0.0086	-0.0089
37V	214.26	214.40	214.40	-0.3502	-0.0500	-0.0508
37H	154.20	154.20	154.21	0.0552	0.0453	0.0444
W_B	5.165	5.238	5.239	-0.2273	-0.0679	-0.0679

Table 4. Means and trends for the raw (no adjustment), regression-adjusted, and exact T_B (K and K/decade) and W_B (mm and mm/decade).
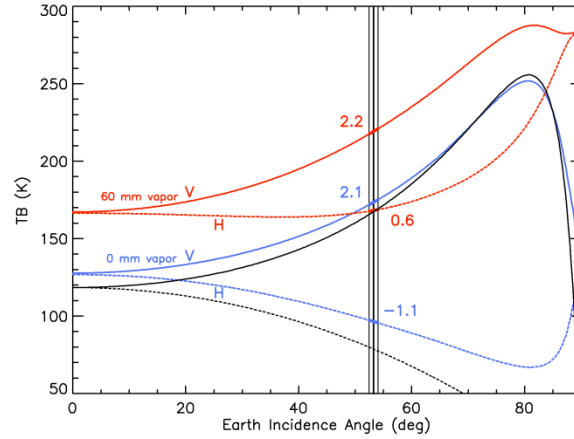
Figure 1. Brightness temperature at 19.35 GHz versus earth incidence angle for vertical (solid) and horizontal (dashed) polarization. The blue curves are for 0 mm of water vapor and the red curves are for 60 mm of water vapor. The nominal 53.25° SSM/I earth incidence angle is shown by the thick vertical line, and the thin vertical lines show the minimum and maximum SSM/I earth incidence angles. The numbers on the plot are the change in brightness temperature with earth incidence angle (K/deg). The thin black curves are the Fresnel specular emissivity times 273 K.
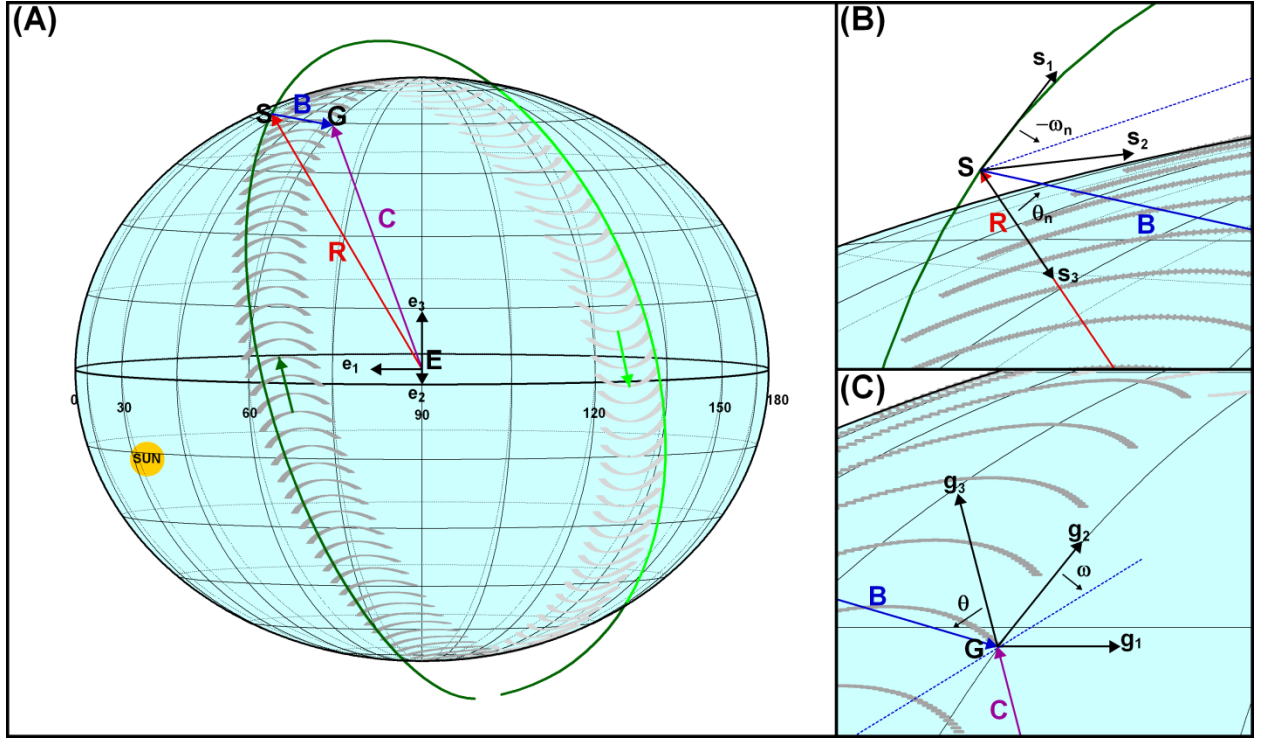
Figure 2. A realistic schematic of the angles and vectors involved in calculating earth incidence angle based on F13 data from 2 January 2003. The coordinate systems are discussed in the text. **(Panel A)** The satellite *S* is orbiting the Earth *E* looking at the ground *G*. The satellite position vector **R** points from the center of the earth *E* to the satellite *S*. The boresight vector **B** points from the satellite *S* to the point on the Earth where it intersects the surface *G*. The resultant $\mathbf{C} = \mathbf{R} + \mathbf{B}$ points from *E* to *G* and is the position vector for the earth-boresight intersection point. The satellite path (green line) and scans sampled every one minute (grey arcs) are depicted with darker colors in front of the earth (ascending orbit portion) and lighter colors behind the earth (descending orbit portion). The sun is behind the earth, and the local equatorial crossing time of the ascending node is 6:19 PM for this example. Longitude (ºE) increases from left to right, and the earth is rotating counterclockwise viewing the north pole from above. The satellite is looking at the last of 64 cells across the swath. **(Panel B)** A close-up on the satellite *S* showing the satellite coordinate system. The boresight vector **B** is projected into the $\mathbf{s_1}$-$\mathbf{s_2}$ plane (blue

dashed line) and the angle between this projection and $\mathbf{s}_1$ is the boresight azimuth angle ω_n; depicted here in the negative direction. The angle between the $\mathbf{s}_3$ axis and $\mathbf{B}$ is the boresight nadir angle θ_n. **(Panel C)** A close-up of the boresight-earth intersection point G. The boresight vector $\mathbf{B}$ is projected into the $\mathbf{g}_1$-$\mathbf{g}_2$ plane (blue dashed line) and the angle between this line and $\mathbf{g}_2$ is the earth azimuth angle ω. The earth incidence angle θ is the angle between $\mathbf{B}$ and $\mathbf{g}_3$.
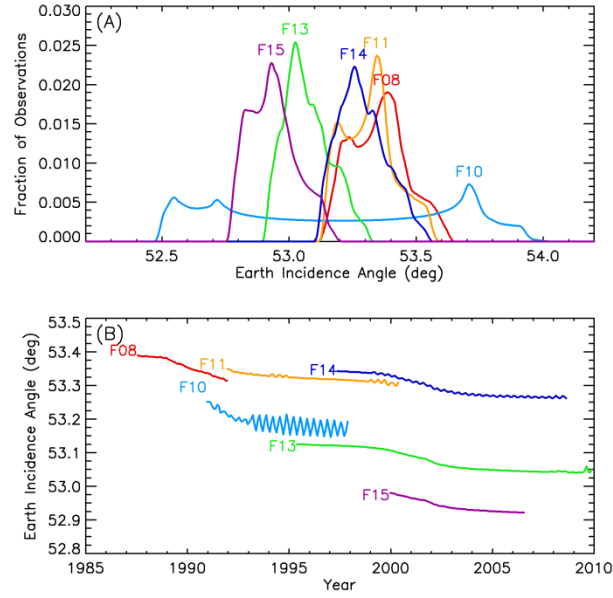
Figure 3. (A) Earth incidence angle histograms for all SSM/I (F08: red, F10: blue, F11: orange, F13: green, F14: dark blue, F15: purple). **(B)** Global monthly-average time series of earth incidence angle for all SSM/I using the same color scheme as above.
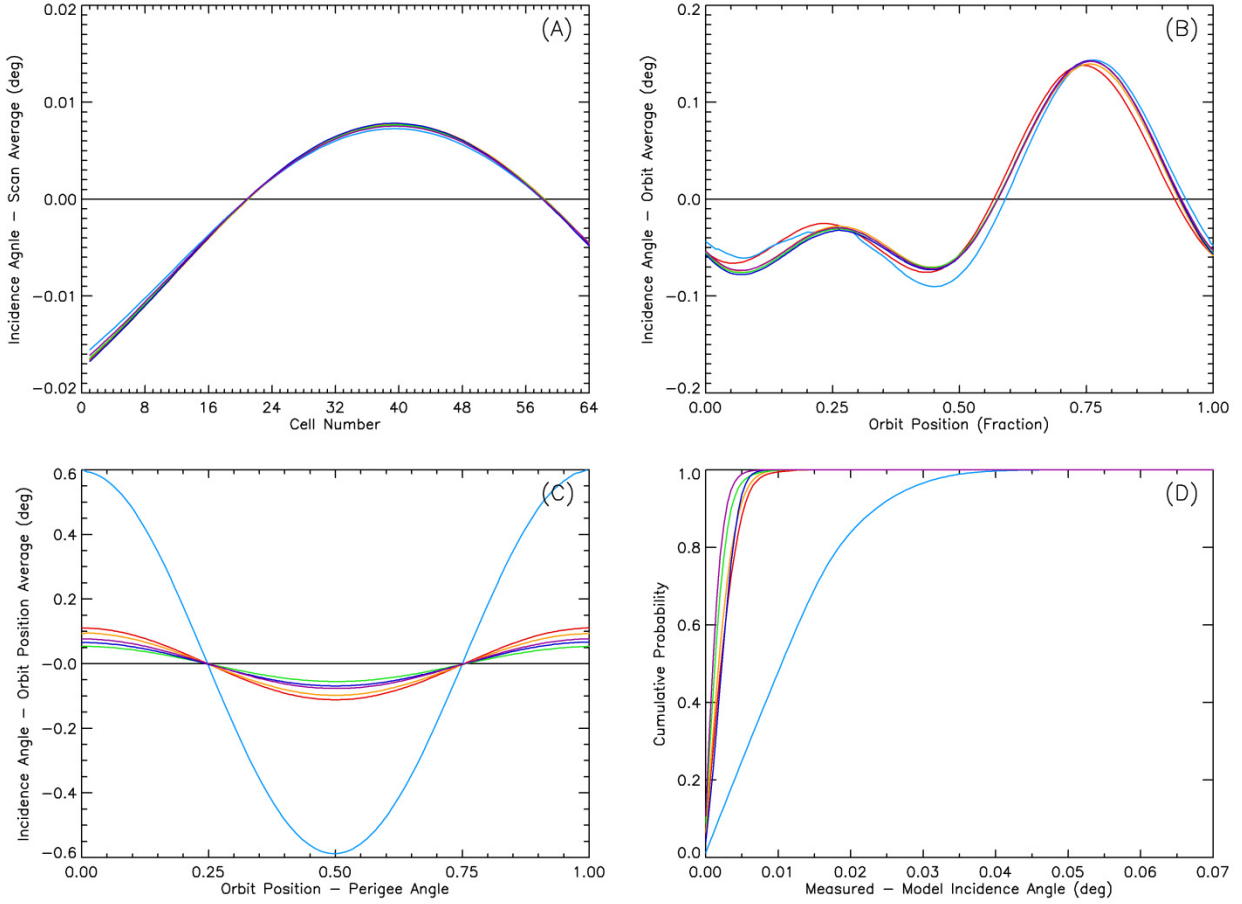
Figure 4. Earth incidence angle characterization for all six SSM/I using the same color scheme as Fig. 3. See the text in Section 4 for more details. **(A)** Earth incidence angle anomaly (scan average removed) as a function of the 64 cells along the scan. **(B)** Earth incidence angle anomaly (orbit average removed) as a function of orbit position. **(C)** Earth incidence angle anomaly (orbit position average removed) as a function of the orbit position minus the perigee angle. **(D)** Cumulative probability that the absolute value of the measured minus model earth incidence angle is less than a certain value.
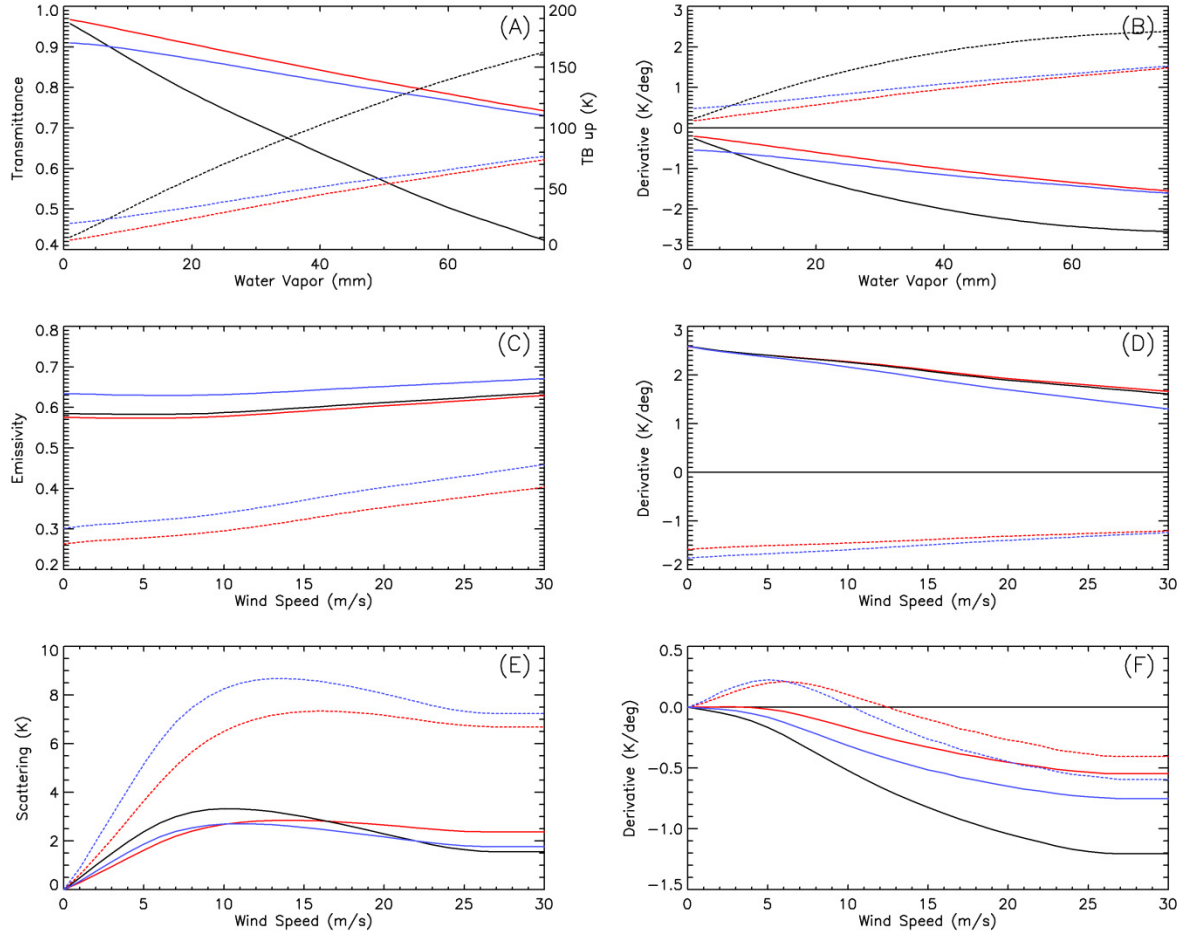
48

Figure 5. Plots of earth incidence angle dependent parameters in the RTM for 19 GHz (red), 22 GHz (black), and 37 GHz (blue). Panel **(A)** shows τ (solid) and T_{BU} (dash) vapor. Panel **(B)** shows $T_S\,\partial\tau/\partial\theta$ (solid) and $\partial T_{BU}/\partial\theta$ (dash) versus vapor. Panel **(C)** shows E_V (solid) and E_H (dash) versus wind speed. Panel **(D)** shows $T_S\,\partial E_V/\partial\theta$ (solid) and $T_S\,\partial E_H/\partial\theta$ (dash) versus wind speed. Panel **(E)** shows S_V (solid) and S_H (dash) versus wind speed. Panel **(F)** shows $\partial S_V/\partial\theta$ (solid) and $\partial S_H/\partial\theta$ (dash) versus wind speed. Panels (E) and (F) are for 30 mm of water vapor.
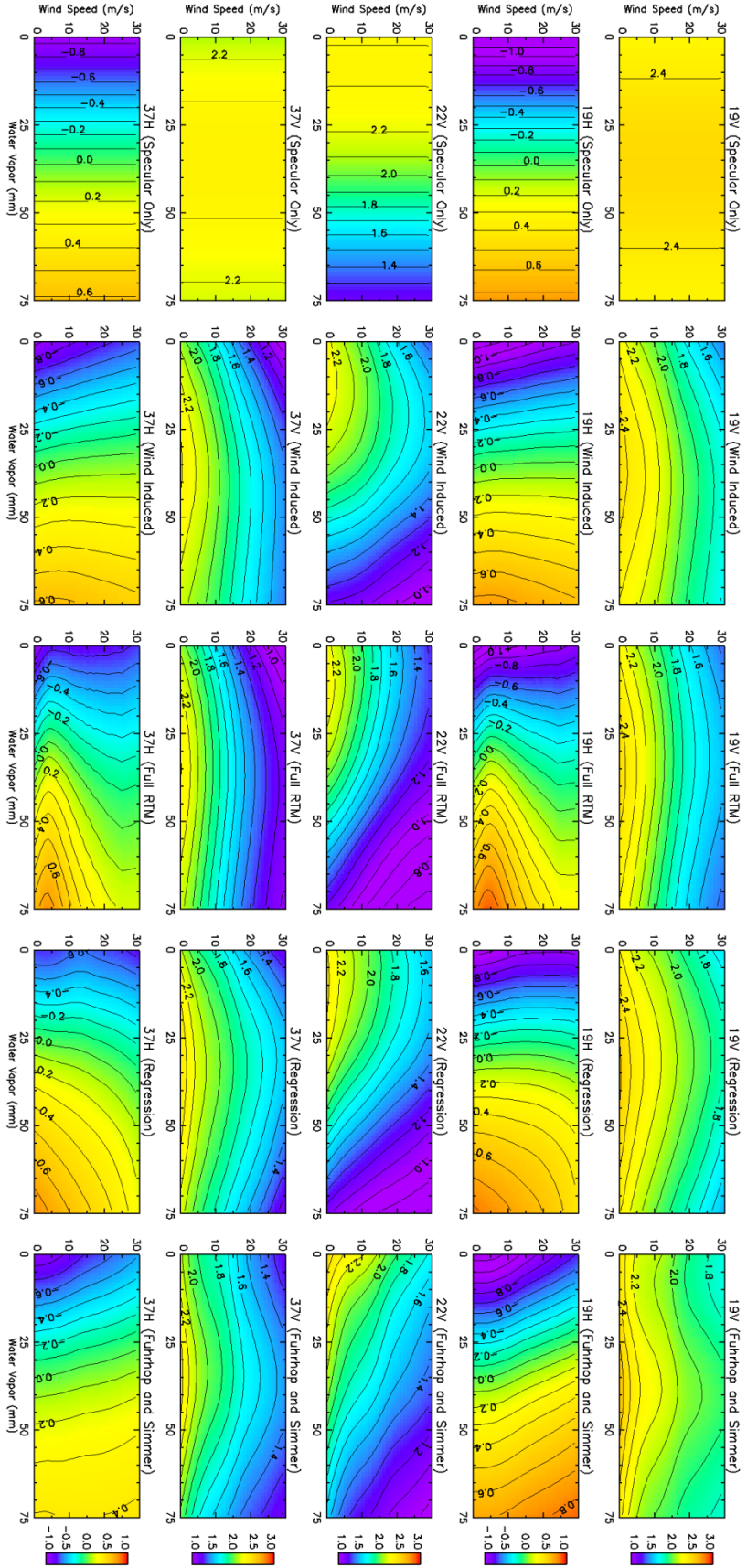
Figure 6. $\partial T_B / \partial \theta$ versus water vapor and wind speed for each channel (19V, 19H, 22V, 37V, 37H from top to bottom). **Column 1** (leftmost) shows $\partial T_B / \partial \theta$ using just the Fresnel specular emissivity and no nonspecular reflection of downwelling radiation. **Column 2** (second from the left) shows $\partial T_B / \partial \theta$ using the specular and wind induced emissivity. **Column 3** (middle column) shows $\partial T_B / \partial \theta$ using the full emissivity and includes nonspecular reflection of downwelling radiation. **Column 4** shows $\partial T_B / \partial \theta$ predicted by the regression derived in this paper. **Column 5** (rightmost) shows $\partial T_B / \partial \theta$ predicted using the *Fuhrhop and Simmer* [1996] regression. For columns 4 and 5, the brightness temperature input required by the regressions is specified using the RSS RTM.
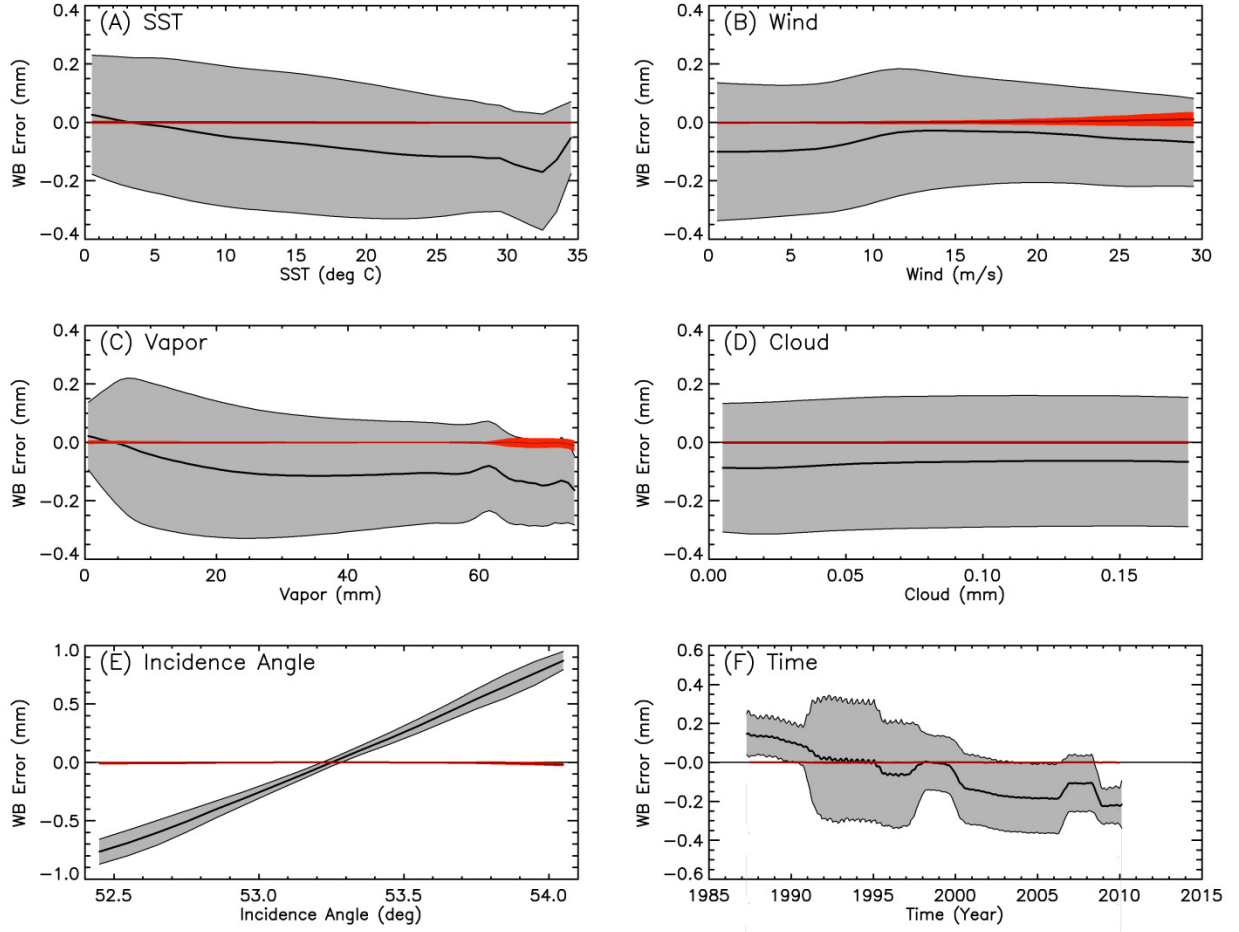
Figure 7. Errors in W_B before adjustment (black/grey) and after adjustment (light/dark red) as a function of: **(A)** sea surface temperature, **(B)** wind speed, **(C)** water vapor, **(D)** cloud water, **(E)** earth incidence angle, and **(F)** time. The bias in the raw unadjusted W_B is shown by the black line and ±1 standard deviation is shown by the grey envelope. The bias in the regression adjusted W_B is given by the dark red line and ±1 standard deviation is given by the red envelope.
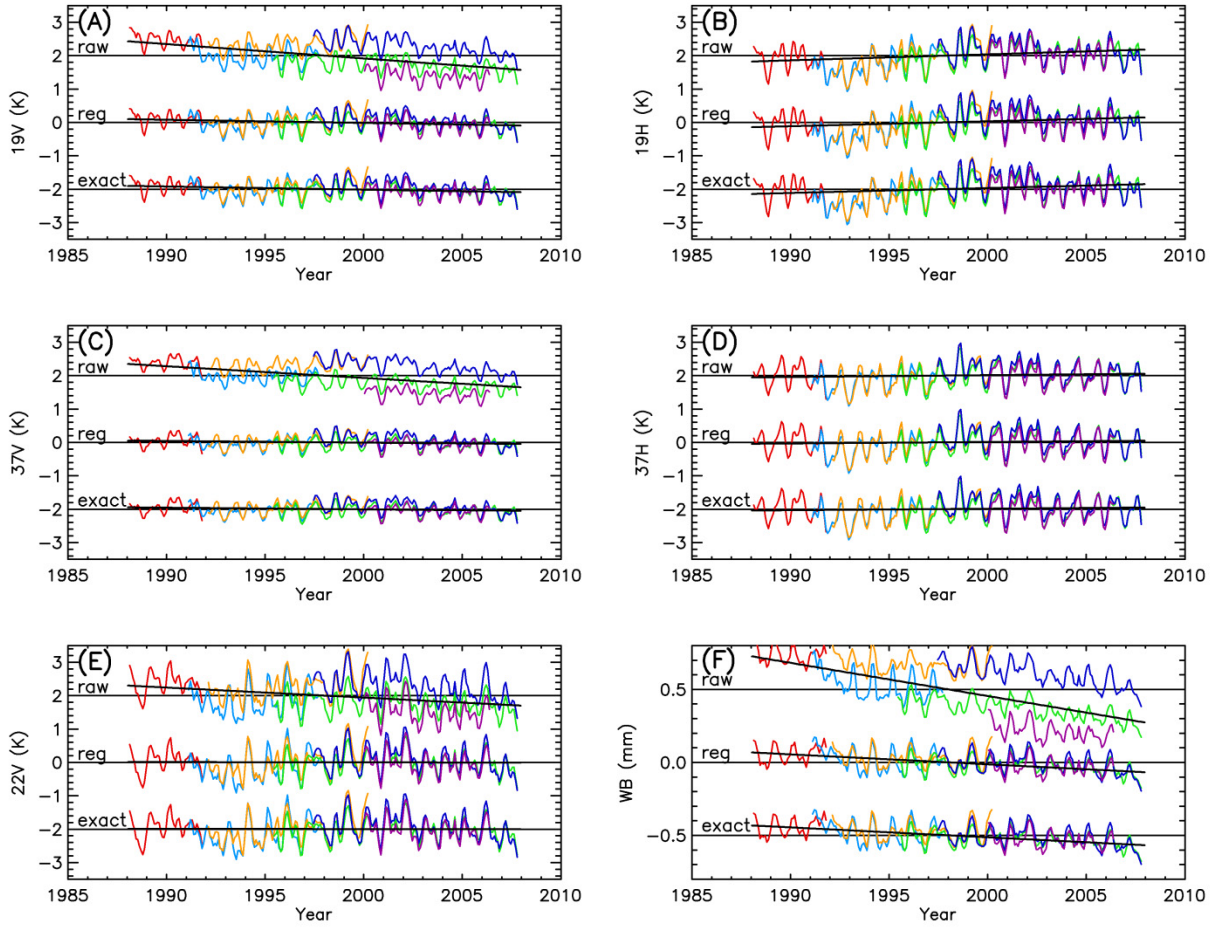
Figure 8. Time series of **(A)** 19V T_B, **(B)** 19H T_B, **(C)** 37V T_B, **(D)** 37H T_B, **(E)** 22V T_B, **(F)** W_B for each SSM/I (same color scheme as Fig. 3) with the mean removed. Within each panel, the top set of lines are the raw values (offset by 2 K for (A)-(E) and 0.5 mm for (F)); the middle set are the regression adjusted; and the bottom set use the exact adjustment from the RTM (offset by -2 K for (A)-(E) and -0.5 mm for (F)). The heavy black lines are the best-fit linear trend. The means and trends are in Table 4.